The Galactic Chemical Evolution of Carbon: Implications for Stellar Nucleosynthesis

Daniel A. Boyea,[1]* James W. Johnson,[1] Third Author[2,3] and Others[1,3]

[1]*Department of Astronomy, the Ohio State University, 191 W. Woodruff, Columbus, OH 43210, USA*

ABSTRACT

C is an important element across astronomy; however, its origin remains poorly understood. We aim to constrain the stellar yields of C through multi-zone Galactic chemical evolution models by comparing predictions with APOGEE subgiants abundances. We find that [C/Mg]-[Mg/Fe] is an emirical estimate of the delayed C sources, enabling us to estimate that AGB stars and CCSNe produce about 20% and 80% of C, respectively. The [C/Mg]-[Mg/H] trend instead represents the equilibrium abundances of C and Mg. We use the [C/Mg]-[Mg/H] trend to estimate the CCSNe C/Mg yield, determining that $y_C^{cc}/y_{Mg}^{cc} = EQUATION$ when including AGB C. Our models are relatively independent of uniform scaling of yields and outflows, and alternate star formation histories. However, the stars which contribute to AGB C production and the SNe Ia delay time distribution of Fe contribute uncertainties to our conclusions. While reliable gas-phase and low-metallicity measurments of C are challenging, we find that our model and a singlezone model with our recommended yields replicate the broad trends of [C/Mg]-[Mg/H]across different environments and metallicities.

1 INTRODUCTION

Carbon is a distinctive and well-studied element in astronomy. Formed in the cores of stars during He fusion, C is the lightest directly synthesized element after He, one of the only light elements formed in low-mass stars, and one the most abundant metals (e.g. Johnson 2019; Karakas & Lattanzio 2014).[1] C structurally changes the environments it pollutes—regulating stellar evolution, facilitating the formation of stars and planets, and forming the basis of earthly life. As such, understanding the origin of C has wide ranging implications. While we know both lower-intermediate-mass and high-mass stars produce C, the relative importance of each process is still unknown.

Galactic chemical evolution (GCE) is a powerful tool, capable of uncovering the origins of the elements. Each enrichment process has characteristic chemical signatures and timescales, enabling us to reconstruct chemical histories. Many previous works have used GCE in attemt to understand C abundances, whether through using theoretical stellar models (Dearborn et al. 1978; Prantzos et al. 2018; Chiappini et al. 2003) or understanding observation (Tinsley 1979; Henry et al. 2000; Bensby & Feltzing 2006; Rybizki et al. 2017; Berg et al. 2019; Kobayashi et al. 2020). (See also review in Romano 2022.) Every study agrees that C is produced by a combination of high-mass and lower-intermediate mass stars, different studies disagree on which process is dominant. For example CITES conclude high-mass stars dominate whereas CITES conclude lower-intermediate mass stars contribute the majority of C. C is also generally understood to have strong metallicity dependent CCSNe enrichment.

One of the primary uncertainties of GCE models are nucleosynthetic yields. Yield predictions – the amounts of each chemical element stars produce – are shaped by poorly understood processes, including mass loss, nuclear reaction rates, rotational mixing, con-

vection, and explodability (Romano et al. 2010; Karakas & Lattanzio 2014; Ventura et al. 2013; Limongi & Chieffi 2018; Griffith et al. 2021). To better understand where C comes from and how it evolves, our aim is to combine APOGEE observations and multi-zone models to develop observationally-consistant yields. Johnson et al. (2023) examined similar GCE models of N (which is closely related to C), finding that trends in N and O are explained by the metallicity dependence of N/O yields. Johnson et al. (2023) determine that AGB N abundances roughly dependence on metallicity (i.e. $y_N/y_O \propto Z$). Here, we extend their models to C, deriving similar constraints on C/Mg yields. We assess which yield prescriptions reproduce Galactic abundance trends while investigating the impact of GCE model assumptions, such as the star formation history (SFH) and outflow mass loading.

We know, from observations of MW stars and extragalactic gas measurments, that C/O traces a banana shape in O/H (see Fig. 10 and section 5.7). C (and O) have been observed in local and extragalactic HII regions (CITES), dwarf galaxies (Berg et al. 2019, e.g.), halo and thick disc Milky Way stars (e.g. Fabbian et al. 2009; Nissen et al. 2014; Lambert & Ries 1981; Laird 1985; Lambert et al. 1986), and damped Lyman-alpha systems. [2] The many observations of C and O paint a broadly consistant picture of a global trend. At the very lowest metallicities, where $[O/H] \lesssim -2$,[3] observations suggest that C/O declines with metallicity. From $-2 \lesssim [O/H] \lesssim -1$, C/O is roughly constant with metallicities. And, at higher metallicities $-1 \lesssim [O/H]$, C/O increases with increasing metallicity.

However, observations of C are not without challenges. As stars ascend the red giant branch (RGB) at the end of H core burning,

---

[1] By metallicity, we mean the (mass) fraction of any element which is not H or He, denoted by Z. For the sun, we take $Z_\odot = 0.014$.

[2] DLAs; high redshift clouds of gas observed as absorption lines in yet higher redshift quasars

[3] In this paper, we use the standard notation for chemical abundances. $[A/B] = \log_{10}(A/B) - \log_{10}(A_\odot/B_\odot)$, i.e. $[A/B]$ is the logarithm of the ratio between A and B, scaled such that $[A/B] = 0$ for the sun. Solar abundances are as measured in Asplund et al. (2009).

C abundances are modified through *first dredge up*[4]. Because the effects of first dredge up are mass-dependent, C and N abundances are frequently used as age indicators for RGB stars (Masseron & Gilmore 2015; Martig et al. 2016; Hasselquist et al. 2019; Vincenzo et al. 2021). Evolved RGB stars thus require modelling-dependent corrections to recover birth C and N abundances (e.g. Vincenzo et al. 2021). C is also challenging to determine in optical spectroscopy. C lines are relatively faint, and surveys such as GALAH struggle against low detection rates, potentially biasing sample measurements. (e.g. gaia-eso AS WELL Franchini et al. 2020). In the gas phase, HII regions are our best window into C abundances. Unfortunately, C lacks strong collisional excitation lines, and recombination lines fall in the ultraviolet without nearby reference H lines (Skillman et al. 2020). Recombination-line and collisional-excitation-line measurements furthermore disagree by a factor of ∼2 (García-Rojas & Esteban 2007).

As our primary observational constraint, we use a sample of subgiant stars from the APOGEE (Majewski et al. 2017) selected by the criteria in Roberts et al. (2023, in prep; see Appendix A). According to stellar evolution theory and observations (Gilroy 1989; Korn et al. 2007; Lind et al. 2008; Souto et al. 2018, 2019), these stars have not yet experienced first dredge up yet have well-mixed envelopes. So, subgiant surface abundances most accurately represent their birth composition. INTRO TO APOGEE takes high-resolution near-infrared spectroscopic measurments of stars, allowing accurate determination of chemical abundances and stellar parameters. In particular, near-infrared C abundances are more reliable than in optical spectroscopy (CITE??). Fig. 1 shows the subgiant sample plotted in [C/Mg]-[Mg/H] and [C/Mg]-[Mg/Fe]. [C/Mg] increases with metallicity, and [C/Mg] decreases with [Mg/Fe] at fixed [Mg/H]. Using the subgiant abundance trends, we will develop a model of the enrichment sources and evolution of C.

2 NUCLEOSYNTHESIS

Yields – the amounts of each chemical element stars synthesise – are central to studies of galactic chemical evolution (GCE). In this section, we compare literature yield predictions and discuss our fiducial yield choices. We focus on three nucleosynthetic pathways: asymptotic giant branch (AGB) stars, core collapse supernovae (CCSNe), and type Ia supernovae (SNe Ia). C is produced in both AGB and CCSNe stars. We also use Mg and Fe as tracers of CCSNe and SNe Ia enrichment respectively. O and Mg are produced almost entirely from CCSNe with metallicity-independent yields. In contrast, Fe is produced in similar amounts by CCSNe and SNe Ia.

After a single stellar population (SSP)[5] forms, CCSNe are the first chemical enrichers. CCSNe explode within ≲ 40 Myr, providing light elements (e.g. C, O, and Mg) and heavier elements (Fe and beyond). Next, low-mass stars begin to reach the end of their lives, entering the AGB phase. By shedding their outer layers, AGB stars are important sources of C, N, and neutron capture elements. Finally, white dwarfs explode in SNe Ia, releasing Fe and other iron-peak elements.

To quantify yields, we define the stellar yield to be the fraction of a

---

Table 1. Yields for the fiducial model (in units of SSP birth mass). See Section 2.1 for the definition of C11.

Element	y^{cc}	$ʎ^{agb}$	y^{ia}
C	Eq. 17	$2.9 \times$ C11	0
O	0.015	0	0
Mg	0.00185	0	0
Fe	0.0012	0	0.00214
N	0.00072	$0.0009 M \left(\frac{Z}{Z_\odot} \right)$	0

stars initial mass which is newly synthesized and released as a given element. For an element X and star with mass M, the net-fractional stellar yield $ʎ$ is

$$ʎ_X = \Delta Z_X \frac{M_{\text{ejected}}}{M_{\text{birth}}} \tag{1}$$

where M_{ejected} and M_{birth} are the total ejected mass and the birth mass of the star, and ΔZ_X is the change in Z_X from the birth material to the ejected material of the star.[6] For example, a $1 \, M_\odot$ star with $ʎ_C = 10^{-3}$ will add $10^{-3} \, M_\odot$ of new C to the interstellar medium. Also, note that yields may be negative if the material returned to the interstellar medium has a lower abundance Z_X than the material the star was formed from. Although per-star yields are necessary to compute AGB star enrichment rates in GCE models, initial-mass-function (IMF) averaged yields are useful in interpreting their predictions. An IMF-averaged yield adds together the yields of stars of each mass, weighted by the fraction of stars of each mass (the IMF). Given the fractional yield $ʎ(M, Z)$ as a function of initial stellar mass M and metallicity Z, the IMF-averaged yield is given by

$$y_X(Z, t) = \frac{\int_{M_{\text{min}}(t)}^{M_{\text{max}}} ʎ_X(M, Z) \frac{dN}{dM} M \, dM}{\int \frac{dN}{dM} M \, dM} \tag{2}$$

where dN/dM is the IMF, $M_{\text{max}} = 100 \, M_\odot$ is the maximum stellar mass, and $M_{\text{min}}(t)$ is the mass of stars with lifetime t.[7] To calculate the IMF-averaged net yields, we use the Versatile Integrator for Chemical Evolution code (vice).[8]

We adapt the yield choices of elements besides C from Johnson et al. (2021, 2023). Table 1 contains our fiducial yields. Following Johnson et al. (2021, 2023), we also take the SNe Ia delay time distribution to be a $t^{-1.1}$ power-law with a minimum delay time of 140 Myr, as suggested by the observations of Maoz et al. (2012).

2.1 Asymptotic Giant Branch Stars

An AGB star is a low-mass ($\lesssim 8 M_\odot$) star during its final phase of evolution. Inside an AGB star, an inert CO core is surrounded by thermally-unstable He and H-burning shells below a convective envelope. In an AGB star, two competing processes determine the outcome of C production: *third dredge up* and *hot bottom burning*. Third dredge up accompanies thermal pulses in AGB stars, where material from the CO core is mixed with the envelope, increasing surface C abundances (Karakas & Lattanzio 2014). The C yields of the star are increased as this C-enhanced envelope is released to the

---

[4] First dredge up is when material from CNO processed core is mixed with the (convective) stellar envelop during the ascent onto the RGB. As a result, C is decreased and N is increased depending on the strength of this process and the envelop mass.

[5] SSP: Single stellar population. Technical name for a group of stars born in the same conditions at the same time, i.e. an open cluster.

[6] Z_X represents the mass fraction of element X.

[7] In our model, the mass-lifetime relation is $\log \tau_M = 1.02 - 3.57 \log M + 0.90 (\log M)^2$, where τ_M is in Gyr, from Larson 1974. We use $t_{\text{end}} = 10 \, \text{Gyr}$ for total yields when t is not used.
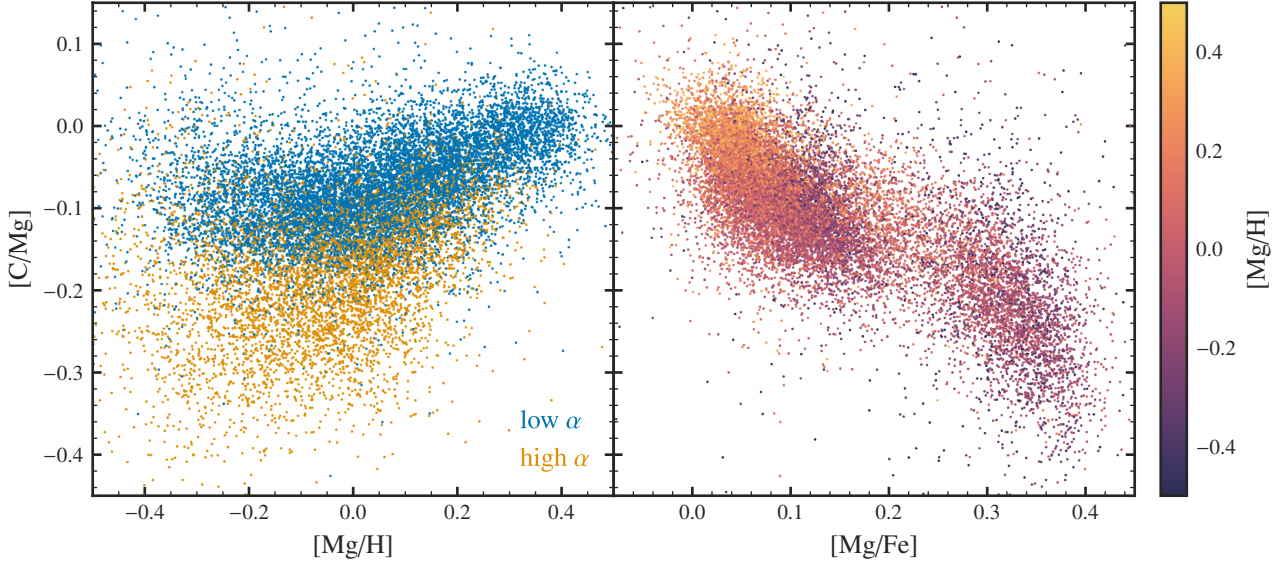
[8] vice is available at https://github.com/giganano/VICE

Figure 1. The [C/Mg] ratio against [Mg/H] (top) and [Mg/Fe] (bottom) for the Roberts et al. (2023, in prep.) sample of APOGEE subgiants. On the top, we plot high and low-α stars in blue and orange, using the separation defined in Equation A2 (the high and low-α stars are named for their high or low α-element to Fe ratios, or in this case, Mg/Fe). On the bottom, we colour-code stars according to their [Mg/H] abundance.

interstellar medium. Hot bottom burning is the activation of the CNO cycle[9] at the bottom of the convective envelope when $T \gtrsim 50\,\mathrm{MK}$. Because the ^{14}N proton capture is the slowest component of the CNO cycle, the CNO cycle converts nearly all ^{12}C into ^{14}N (Adelberger et al. 2011).

Hot bottom burning and third dredge-up result in mass-dependent C yields. Stars less than $\sim 2\,\mathrm{M_\odot}$ do not experience third dredge-up. As a result, these stars C abundances are only affected by first dredge-up, resulting in little change to C yields or slight destruction of C. Between ~ 2 and $\sim 5\,\mathrm{M_\odot}$, third dredge up becomes important, enriching the outer layers with C, making these stars the most important producers of C. In AGB stars more massive than $\sim 5\,\mathrm{M_\odot}$, both hot bottom burning and third dredge up occur; however, hot bottom burning is much more efficient, resulting in significant ^{12}C destruction.

In this work, we explore four different sets of AGB star yield tables from literature, providing necessary well-sampled grids in mass and metallicity. We refer to the yields from the following studies as the following,

C11: Cristallo et al. (2011, 2015)
K10: Karakas (2010)
V13: Ventura et al. (2013, 2014, 2018, 2020)
K16: Karakas & Lugaro (2016); Karakas et al. (2018)

In Appendix B, the masses, metallicites, and notable differences between each yield set are briefly described. For our models to match observations, we find that need to uniformly amplify these yield tables. We use C11 table, amplified by a factor of 2.9, as the fiducial AGB yield.

Fig. 2 compares the stellar AGB C yields for these four models.

Most models agree on the qualitative shape of the net fractional AGB C yield. Stellar yields peak between masses of about 2–4 $\mathrm{M_\odot}$ and decline as stars become more or less massive. As metallicity increases, the total AGB C yield decreases. The mass of peak C yields also increases slightly with metallicity. Metal poor stars dredge up more material due to the decreased power of the CNO cycle, resulting in increasing carbon yields with decreasing metalicity (Ventura et al. 2013).

Fig. 3, on the left, shows the total production of C by AGB stars in a SSP at an age t, i.e. $\dot{x}_C(Z_\odot, t)$. As the mass range $2\,\mathrm{M_\odot} \lesssim M \lesssim 4\,\mathrm{M_\odot}$ is most important for C production, about half of C production occurs before ~ 1 Gyr, similar to SNe Ia Fe. K10 and K16 weight C production more heavily towards high-mass AGB stars resulting in a faster enrichment delay time, whereas the C11 and V13 models predict a slightly longer timescale of ~ 1 Gyr. In any case, little to no C is produced more than 2 Gyr after a star formation event. Fe production, in contrast, continues steadily for 10 Gyr.

The right panel of Fig. 3 shows IMF-averaged C yields for each AGB model as a function of metallicity. V13 differs in that it shows a non-monotonic metallicity dependence. However, this effect is only for models with $\log Z/Z_\odot \lesssim -1$. Otherwise, models differ only in their yield normalization and metallicity dependence. All yield models span a range of ~ 2 for a given metallicity. For example, all four models predict $y_C^{\mathrm{agb}}(Z_\odot)$ to be between 0.004 and 0.008 at solar metallicity. The models also differ slightly in the strength of metallicity dependence, with about a factor of 3 discrepency (see Table 2).

2.2 Core Collapse Supernovae

Massive stars form ^{12}C in their cores through the triple–α process.[10] However, only C ejected through supernovae and stellar winds contributes to the yield. While there are many stellar models providing

---

[9] The CNO cycle is a series of proton-capture reactions with CNO elements resulting in energy generation and the creation of an α particle. $^{12}\mathrm{C}(p,\gamma)^{13}\mathrm{N}(\beta^+,\nu_e)^{13}\mathrm{C}(p,\gamma)^{14}\mathrm{N}(p,\gamma)^{15}\mathrm{O}(\beta^+,\nu_e)^{15}\mathrm{N}(p,\alpha)^{12}\mathrm{C}$. There are other less important minor branches of the CNO cycle (Adelberger et al. 2011).

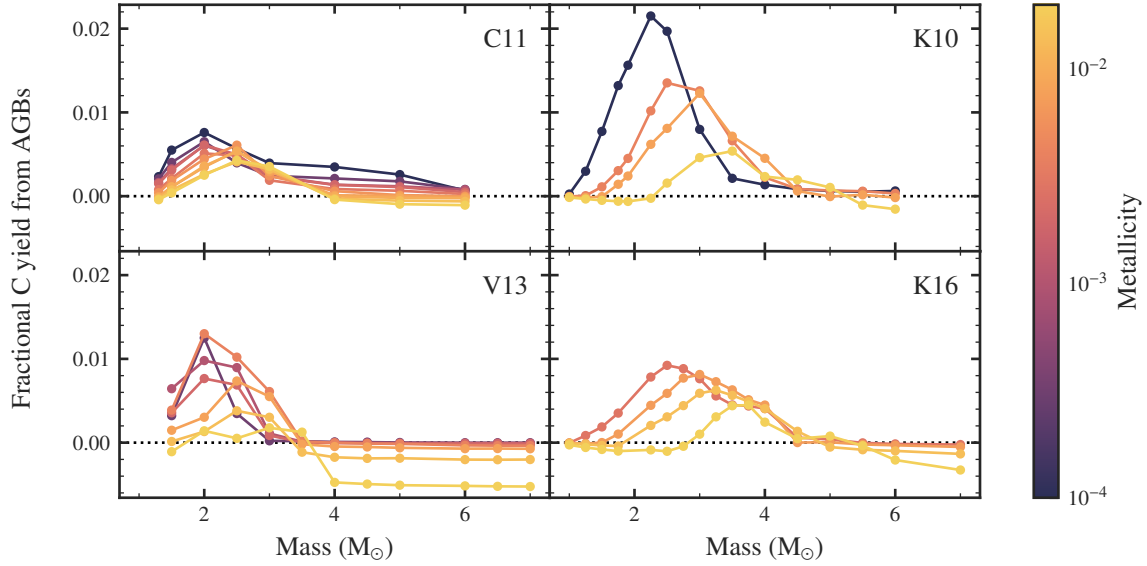[10] The 3-α process fuses 3 He nuclei into O.

Figure 2. The net fractional AGB C yield plotted as a function of initial stellar mass M and colour-coded according to metallicity. The black dashed line shows $\acute{k} = 0$ for reference. Each panel represents yields from one of four AGB models: C11, K10, V13, K16 (see Section 2.1 and Appendix B).
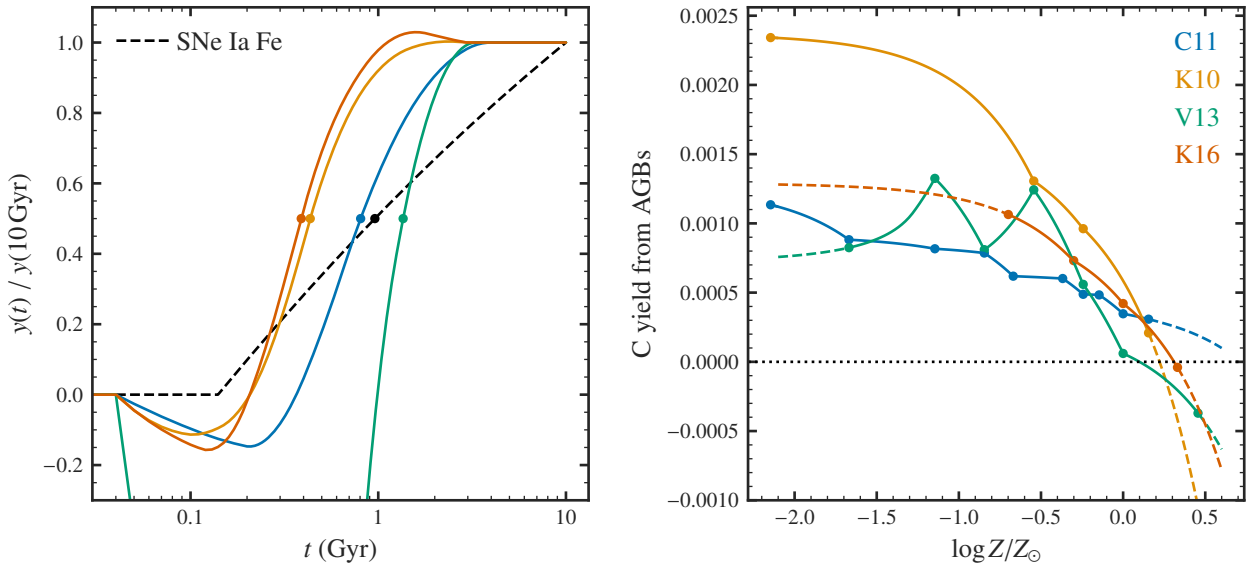

Figure 3. C production by AGB stars as a function of SSP age, normalized to the total mass $M_{\rm tot}$ produced at $t = 10$ Gyr. **Left:** The four AGB yield models from literature at solar metallicity (C11, K10, V13, or K16). The dashed black line shows the delay time distribution of type Ia supernovae ($\propto t^{-1.1}$) for comparison. **Right:** The (IMF-weighted) AGB C yield $y_{\rm C}^{\rm agb}$ as a function of metallicity for each of the AGB yield models. ($y_{\rm C}^{\rm agb}$ is the net mass of C produced by AGB stars per unit mass of star formation, after 10 Gyr and assuming a Kroupa 2001 IMF.)

predictions of CCSNe yields, the results of these models are highly uncertain due to the complexity of stellar modeling.

Fig. 4 plots calculations of the IMF-integrated yields, defined with Eq. 2 (computed using VICE's `vice.yields.ccsne.fractional` function). CCSNe models predict a wide range of C yields, spanning almost a factor of ten. Both the Nomoto et al. (2013) and Limongi & Chieffi (2018) models show positive metallicity dependence. As metallicity increases, stars lose more of their mass to winds. In particular, C enriched envelop material is lost through winds before synthesized into heavier elements, so C yields can be strongly metallicity dependent (VERIFY). Fig. 4 shows the C11 AGB model for

comparison on the left. Especially at $Z \approx Z_\odot$, most CCSNe models dominate AGB C production. Later, we will also show empirically this is the case. The right of Fig. 4 shows the CCSNe [C/Mg] ratio for the different models, defined by

$$[{\rm C/Mg}]^{\rm CC} = \log_{10}\left(\frac{y_{\rm C}^{\rm cc}}{y_{\rm Mg}^{\rm cc}}\right) - \log_{10}\left(\frac{Z_{\rm C,\,\odot}}{Z_{\rm Mg,\,\odot}}\right). \tag{3}$$

If only CCSNe produced C, then $[{\rm C/Mg}]^{\rm CC}$ describes the equilibrium abundance of [C/Mg]. Different CCSNe models also span a large range in [C/Mg]. We chose to instead parameterize $y_{\rm C}^{\rm cc}$ to sim-

plify model inputs, as most CCSNe models fail to achieve near-solar [C/Mg].

Both rotation and explodability introduce substantial variations. The Limongi & Chieffi (2018) models include rotation, showing that variations in the rotational velocity of the star can dramatically increase the magnitude and metallicity dependence of y_C^{cc}. Rotation induces more mixing allowing the CO core to grow larger and contributes to wind losses. As we will later show, CCSNe C production needs to be strongly metallicity-dependent at $Z/Z_\odot \approx 1$, which is consistent with the Limongi & Chieffi (2018) rapidly rotating models. Assumptions about the explodability landscape affect C and Mg production. As fewer high-mass stars explode, both C and Mg yields decrease, but Mg yields decrease more as more C is lost to winds, so [C/Mg] increases with decreasing explodability.

O and Mg are both α-elements, light elements produced in CCSNe through He-nuclei fusion. As we focus on constraining relative yields, we neglect O and Mg yield variations in the main text (excluding the uniform scaling of yields and massloading in Section 5.6). There is substantial variation in predicted Mg yields. Most models predict relatively flat trends metallicity (even with rotation as in Limongi & Chieffi 2018). However, the variation is significant and our adopted y_{Mg}^{cc} yield is much higher than most models, but O and Mg yields of CCSNe models do not fully match observations. CCSNe models underpredict [Mg/O], and the reason why is unknown (see e.g. Griffith et al. 2021). Here, we assume [O/Mg] = 0, which nevertheless consistent with APOGEE observations (Weinberg et al. 2019, 2022).

3 ANALYTIC APPROXIMATIONS

In this section, we describe approximations of galactic abundance trends and C yield models. While these are insufficient to describe the galaxy in full detail, we can use these simplified models to inform our investigation.

3.1 Equilibrium Abundances

Galaxies, when moderated by metal-poor gas accretion and feedback-driven outflows, reach a chemical equilibrium. The production of new metals is balanced by losses to new stars and outflows (Larson 1972; Dalcanton 2007; Finlator & Davé 2008; Peeples & Shankar 2011; Lilly et al. 2013). While our galaxy is likely not in perfect equilibrium or described by a single, homogeneous chemical envirnoment, the equilibrium approximation is nevertheless useful in understanding yields and metallicity dependence of solar neighborhood stars (e.g. Johnson et al. 2022, 2023; Weinberg et al. 2017).

Here, we assume a simple *one-zone* chemical evolution model (e.g. Tinsley 1980; Pagel 2009; Matteucci 2021). Newly produced metals are homogeneously and instantaneously mixed, so this model evolves as a single, spatially-uniform chemical zone. We define M_X to be the gas mass of element X, $\dot{M}_\star$ to be the star formation rate (in $M_\odot\ yr^{-1}$), and η to be the mass loading factor $\eta \equiv \dot{M}_{outflow}/\dot{M}_\star$ (representing the strength of outflows). A SSP returns a fraction r of their birth mass to the interstellar medium, due to ejected stellar envelopes.[11] Here, we will use α as a representative α-element, such as O or Mg. Given the IMF-averaged yield y_α, the rate of change in the gas-phase mass of α is a sum of sources and sinks,

$$\dot{M}_\alpha = y_\alpha \dot{M}_\star - \dot{M}_{\alpha,\,remnants} - \dot{M}_{\alpha,\,outflows} \tag{4}$$

where $y_\alpha \dot{M}_\star$ describes CCSNe enrichment. In terms of the return mass fraction of stars r, the mass lost to remnants is $Z_\alpha \dot{M}_\star (1 - r)$. And, the outflows deplete mass at a rate $Z_\alpha \dot{M}_\star \eta$. (We assume the composition of outflows is the same as the interstellar medium.) With these definitions, Eq. 4 becomes

$$\dot{M}_\alpha = y_\alpha \dot{M}_\star - (1 + \eta - r) Z_\alpha \dot{M}_\star. \tag{5}$$

Assuming an exponentially declining star formation history (SFH) $\dot{M}_\star \propto e^{-t/\tau_{sfh}}$, the equilibrium abundance is derived analytically by setting $\dot{Z}_\alpha = 0$.

$$Z_\alpha^{eq}(R) = \frac{y_\alpha}{1 + \eta(R) - r - \tau_\star/\tau_{sfh}}, \tag{6}$$

where $\tau_\star$ is the star formation rate. (η depends on R to create a metallicity gradient. See also Section 4 and Eq. 20.) In the special case of constant star formation, $\tau_{sfh} \rightarrow \infty$ and the denominator simplifies to $1 + \eta - r$.

Likewise, for C production, where both AGB stars and CCSNe play a role,[12] Eq. 6 then becomes

$$Z_C^{eq}(R) = \frac{y_C^{cc} + y_C^{agb}}{1 + \eta(R) - r - \tau_\star/\tau_{sfh}} \tag{7}$$

The equilibrium C/α abundance ratio is then

$$\frac{Z_C^{eq}}{Z_\alpha^{eq}} = \frac{y_C^{cc} + y_C^{agb}}{y_\alpha}. \tag{8}$$

Analogous to Johnson et al. (2023) arguments about N, the trends in abundance ratios are set by yield ratios in these GCE models. The effect of other GCE parameters (most importantly η) cancels. As a consequence, yield ratios should establish abundance ratio trends in models which assume a different normalization of element yields and mass-loading (see discussion below). This argument can also be inverted to infer yields from abundance ratio trends. To the extent that observed C and α trends reflect the equilibrium abundances in different Galactic regions, we can infer the total C yield.

$$y_C^{cc} + y_C^{agb} = y_\alpha \left(\frac{Z_C}{Z_\alpha}\right)_\odot 10^{[C/\alpha]}. \tag{9}$$

As we know [C/α] as a function of metallicity, Eq. 9 enables us to estimate both the magnitude and metallicity-dependence of y_C/y_α. In Fig. 5, we show the inferred total C yields, based on this equation, and our best fitting linear model. From a linear regression, we suggest that

$$\frac{y_C(Z)}{y_O} \approx \frac{1}{3} + 4 (Z - Z_\odot) \tag{10a}$$

$$\frac{y_C(Z)}{y_{Mg}} \approx 2.7 + 32 (Z - Z_\odot). \tag{10b}$$

These yield ratios results in an equilibrium abundance [C/α] = −0.09, which is consistent with the subgiant sample and is within ~20% of the solar C/Mg mixture from Asplund et al. (2009).

Both observational and theoretical uncertainties limit the accuracy of our relative yield predictions. As the metallicity range of our data is small (−0.4 ≲ [Mg/H] ≲ 0.4), our model does not extend beyond near-solar metallicities. Additionally, the derived yields will be systematically biased if the galaxy is out of equilibrium, for example, due to a recent starburst (Mor et al. 2019; Isern 2019). As we will

---

[11] $r \approx 0.4$ for a Kroupa 2001 IMF.

[12] In detail, the AGB contribution requires integration over the SFH to account for the finite lifetimes of stars. However, for this exponential SFH, this effect is minimal, so we simply use y_C^{agb} for the current AGB contribution.
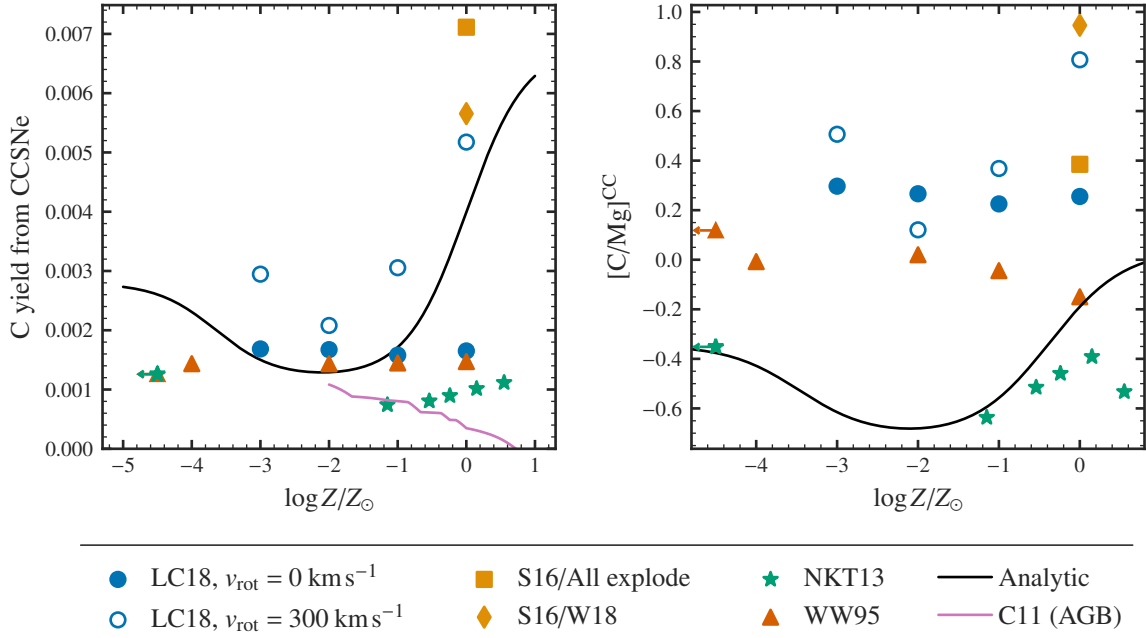
Figure 4. C yields from high-mass stars. **Left** The IMF-weighted CCSNe yield of C as a function of metallicity. **Right** The CCSNe [C/Mg] abundance ratio, defined in Eq. 3. The black line is the derived C yield from Section 3.1, $y_C^{cc} = 0.0028 + 0.001(Z/Z_\odot)$. Yields are shown for tables from Woosley & Weaver (1995, red triangles), Sukhbold et al. (2016, orange squares and diamonds), Nomoto et al. (2013, green stars), and Limongi & Chieffi (2018, blue circles). Sukhbold et al. (2016) report yields for different black hole landscapes, while Limongi & Chieffi (2018) provide yields at different rotational velocities. In the top panel, the pink line denotes y_C^{agb} from C11 for comparison. All models include wind yields. (OUT OF DATE)
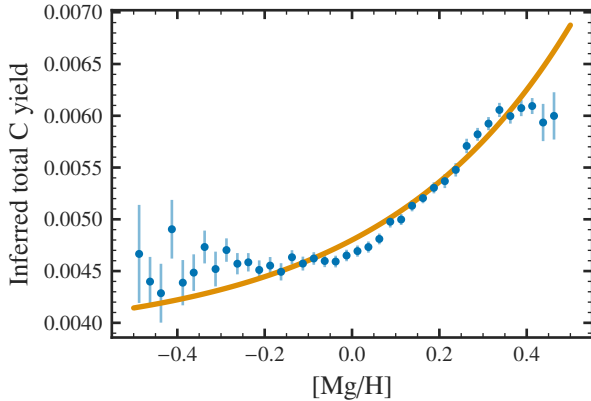
Figure 5. Inferred high-mass star C yields as a function of metallicity. We assume equilibrium and $3 \times$ C11 AGB yields (orange curve, see discussion in Section 3.1). Blue points are the median value of y_C^{cc} for each bin in [Mg/H] with uncertainties based on the 16-84 percentile range.

3.2 Analytic AGB

To parameterize the AGB contribution to C production, we define f_{agb} to be the fraction of C which comes from AGB stars.

$$f_{agb} \equiv \frac{y_C^{agb}(Z = Z_\odot)}{y_C(Z = Z_\odot)}, \tag{11}$$

In Section 5.4, we will show that $f_{agb} \approx 0.2$. None of the AGB yield sets (C11, K10, V13, K16) produce enough C relative to our total y_C^{cc} values. So, we introduce a normalization factor α_{agb}, which denotes a multiplicative scaling of y_C^{agb}

$$y_C^{agb} \rightarrow \alpha_{agb} \, y_C^{agb}. \tag{12}$$

Table 2 contains the required values of α_{agb} to reach $f_{agb} = 0.2$, the yields at solar metallicity, and the metallicity for each AGB yield set.

We can use the [C/Mg]-[Mg/Fe] diagram of APOGEE stars to estimate the delayed portion of C. When binned in metallicity, median [C/Mg] changes by about 0.2 dex across the range of [Mg/Fe] at solar metallicities (see Fig. B1). As high-α stars have little to no delayed SNe Ia Fe, these stars would also have little to no delayed AGB C. This means that AGB C stars make up about at most a fraction $f_{agb} \approx 1 - 10^{-0.2} \approx 0.4$ of C production.

We also briefly explore an analytic AGB model, defined as a cubic piecewise in mass and linear in metallicity. The piecewise is defined to have a maximum at m_1 and minimums at the end points $m - \delta m_-$ and $m + \delta m_+$. The function becomes constant outside of this range

discuss in Section 5.6, the normalization of yields and η is degenerate. If we increase yields and η by a similar factor, equilibrium abundances from Eq. 6 would be unchanged, so our model cannot distinguish changes in both yields and outflows.

Table 2. For each AGB yield set, the IMF-averaged AGB C yield at solar metallicity $y_{C,0}^{agb}$ and the multiplicative factor reaches an AGB contribution of 20% $\alpha_{agb,20}$.

AGB Model	$y_C^{agb}(Z_\odot)$	$\zeta^{agb}(Z_\odot)$	α_{20}^{agb}
C11	4.2E-4	-0.0175	2.4
K10	6.4E-4	-0.059	1.6
V13	2.2E-4	-0.021	4.5
K16	5E-4	-0.029	2.0

with (optionally) negative yields. The mass dependence is

$$\Lambda(m) = \begin{cases} \Lambda_0 & m \leq m_0 - \delta m_- \\ \Lambda_1 + (\Lambda_0 - \Lambda_1) \, f\left(\frac{m_0 - m}{\delta m_-}\right) & m_0 - \delta m_- < m \leq m_0 \\ \Lambda_1 + (\Lambda_2 - \Lambda_1) \, f\left(\frac{m - m_0}{\delta m_+}\right) & m_0 < m \leq m_0 + \delta m_+ \\ \Lambda_2 & m_0 + \delta m_+ \leq m \end{cases} \quad (13)$$

where Λ_1 approximately represents the total IMF-integrated yield, Λ_0 and Λ_1 represent the yields for low-mass and high-mass AGB stars respectively, and

$$f(x) = 3x^2 - 2x^3. \quad (14)$$

For the full equation, we take the above functional form multiplied by a metallicity dependent term, so

$$\Lambda_C^{agb}(m, Z) = \frac{\Lambda(m)}{\int_1^8 m \, \Lambda(m) \, \text{IMF}(m) \, dm} \left(\Lambda_1 + \zeta \left(Z - Z_\odot\right)\right) \quad (15)$$

3.3 CCSNe Carbon Yields

With the total C yield of Eq. 10 and given an AGB C yield, we can derive an observationally-consistant CCSNe C yield.

$$y_C^{cc}(Z_\odot) = y_C(Z_\odot) - y_C^{agb}(Z_\odot) \quad (16a)$$

$$\zeta^{cc} \equiv \frac{dy_C^{cc}(Z_\odot)}{dZ} = \frac{dy_C(Z_\odot)}{dZ} - \frac{dy_C^{agb}(Z_\odot)}{dZ} \quad (16b)$$

This method reduces the number of free parameters of the model and enables all models to match [C/Mg]-[Mg/H] trends in APOGEE sub-giants when considering AGB yields with different metallicity dependences and normalizations. Table 2 contains our adaptive (regression-derived) values of ζ^{agb} and $y_C^{agb}(Z_\odot)$. For example, in our fiducial model, $y_C^{cc} = 0.004 + 0.102(Z - Z_\odot)$. Our full CCSNe C yield model adds a low-metallicity enhancement term, which is insignificant at solar metallicities (e.g. thin disk stars) but enables models in Section 5.7 to match low-metallicity environments. We parameterize low-metallicity enrichment with y_l and Z_l, the yield and transition metallicity for enhanced low-metallicity yields. All-together,

$$y_C^{cc} = y_{C,0}^{cc} + \zeta^{cc} \left(Z - Z_\odot\right) + \frac{2 \, y_l}{1 + Z/Z_l}. \quad (17)$$

4 THE MULTI-ZONE MODEL

Classical, *one-zone* models of chemical evolution assume instantaneous mixing of metals in the star-forming interstellar medium (e.g. Matteucci 2021). This simple framework is a poor approximation of the Milky Way. The Galaxy evolves *inside-out*—where star formation is higher towards the center and in the early universe (Bird et al. 2013). Additionally, stars can migrate several kpc over their lifetimes,

mixing different chemical environments across the galaxy (Bird et al. 2012; Sellwood & Binney 2002). For the rest of this paper, we focus on multi-zone models, which discretize the Galaxy into concentric rings in which stars move between. Our models extends the Johnson et al. (2021, hereafter J21) Milky Way model, run with the publicly available Versatile Integrator for Chemical Evolution (VICE). This model is described extensively in J21 and concisely summarized in Johnson et al. (2023). Here, we provide a brief overview of the relevant model components.

Star formation is set seperately for each zone. The Galaxy is divided into 200 rings, each 100 pc wide representing a single zone. Each ring (or zone) has a separate stellar population and gas supply. We initially assume an inside-out SFH, where the star formation surface density $\Sigma_\star$ is given by

$$\dot{\Sigma}_\star \propto \left(1 - e^{-t/\tau_{rise}}\right) e^{-t/\tau_{sfh}}. \quad (18)$$

$\tau_{rise} = 2$ Gyr describes when the star formation rate reaches a maximum, and τ_{sfh} describes the decay timescale of star formation as a function of radius R. J21 derives $\tau_{sfh}(R)$ through analysis of four integral field spectroscopy surveys in Sánchez (2020). At each R, the SFH is normalized to match the stellar surface density gradient (Bland-Hawthorn & Gerhard 2016) and the total stellar mass reaches 5.17×10^{10} M$_\odot$ (Licquia & Newman 2015). Star formation ends beyond a radius $R = 15.5$ kpc. The gas inflow is calculated to maintain the SFH for each radius and time, using an extension of a Kennicutt-Schmidt law (Kennicutt 1998),

$$\dot{\Sigma}_\star \propto \begin{cases} \Sigma_{gas} & 2 \times 10^7 \leq \Sigma_{gas} \\ (\Sigma_{gas})^{3.6} & 5 \times 10^6 \leq \Sigma_{gas} < 2 \times 10^7 \\ (\Sigma_{gas})^{1.7} & \Sigma_{gas} < 5 \times 10^6 \end{cases} \quad (19)$$

where Σ_{gas} is measured in M$_\odot$ kpc^{-2}. The scaling of this relationship varies with time due to the redshift dependence of $\tau_\star$ in molecular gas observed by Tacconi et al. (2018). We assume a Kroupa (2001) IMF.

To account for radial migration, we use the h277 hydrodynamical simulation results (with simulation parameters as in Bird et al. 2021; see also Christensen et al. 2012; Zolotov et al. 2012; Loebman et al. 2012; Brooks & Zolotov 2014). Each VICE single stellar population (SSP) is matched to an *analog* in H277, chosen to form at a similar time and radius R. By taking the change in radius ΔR of the analogs, the SSPs move to their final radii with a $\sqrt{\text{time}}$ dependence. The $\Delta R \propto \sqrt{\text{time}}$ dependence arises when migration proceeds as a consequence of the diffusion of angular momentum (Frankel et al. 2018, 2020). We do not account for radial gas flows. Using the results of a hydrodynamical simulation without modification limits the free parameters in the model; however, we are limited to one dynamical history. We also explore a normal-distribution random walk migration based on Frankel et al. (2018), without noticeable impacts on our results. All models shown here use the h277-based migration. The full impact of the details of a galaxy's dynamical history on its chemical evolution is still unknown.

As the strength of outflows controls the resulting α-element abundances, J21 create a metallicity gradient by defining

$$\eta(R) = r - 1 + \frac{y_\alpha^{CC}}{Z_{\alpha,\odot}} 10^{(-0.08 \, \text{kpc}^{-1})(R - 4 \, \text{kpc}) + 0.3}. \quad (20)$$

This choice of $\eta(R)$ results in a [α/H] gradient consistent with Milky Way observations (e.g. Hayden et al. 2014; Weinberg et al. 2019; Frinchaboy et al. 2013).

5 RESULTS

5.1 Evolution of Carbon Abundances

Here, we present the time evolution of our fiducial model. In the next sections, we will discuss the choice of parameters and agreement with observations. The fiducial model has the following qualitative characteristics of its C yields.

    C is mostly (∼80%) produced in CCSNe
    CCSNe produce more C at higher metallicities
    AGB stars produce less C at higher metallicities

The fiducial model uses the C11 AGB yield tables uniformly scaled by a factor of 2.9 (see Section 2.1, and Table 1).

Fig. 6 shows time evolution tracks of the fiducial model for [C/Mg]-[Mg/H] and [C/Mg]-[Mg/Fe]. As discussed in Section 3.1, [C/Mg]-[Mg/H] is set by the total C/Mg yields. [C/Mg]-[Mg/Fe] is instead useful in understanding delayed C production. As both Fe and C are delayed elements, [Mg/Fe] steadily decreases after a star formation event, unlike [Mg/H] which quickly reaches equilibrium. All plots showing [C/Mg]-[Mg/Fe] going forward are selected in metallicity such that $-0.15 \leq$ [Mg/H] ≤ -0.05, so metallicity-dependent yields do not affect this plot. The [C/Mg]-[Mg/Fe]-diagram is, in essance, an emperical delay-time-distribution for a single stellar population of C, especially as we assume a $\propto t^{-1.1}$ delay-time-distribution for Fe. Comparing the top and bottom panels of Fig. 6 highlights the differences between [C/Mg]-[Mg/H] and [C/Mg]-[Mg/Fe]. While [C/Mg]-[Mg/H] quickly reaches its final equilibrium distribution (within ∼5 Gyr), [C/Mg]-[Mg/Fe] continues to evolve in both [Mg/Fe] and [C/Mg] until the simulation ends.

    C evolution proceeds as follows, (for a single zone)

(i) CCSNe initially dominate production. As y_C^{cc} has strong metallicity dependence, [C/Mg] increases with time.

(ii) AGB stars contribute delayed C, causing [C/Mg] to increase even faster with [Mg/H].

(iii) [C/Mg] plateaus as C also approaches equilibrium.

(iv) [C/Mg] may decrease due to declining SFH or slightly negative yields from ∼1 M$_\odot$ stars.

Fig. 7 shows f_{agb} calculated from the fiducial model of current effective C yields in the gas phase (using the SFH as a proxy for y_C^{cc}). At early times, CCSNe dominate. As the galaxy evolves, AGB have time to add C, increasing f_{agb}. However, the metal-rich inner regions lower AGB C yields, so these regions never reach as high of a f_{agb} as the outer regions do.

5.2 Data and Sample Selection

Subgiants provide the ideal observational constraint to our model. When a star enters the Red Giant Branch (RGB), material from the CNO-processed core is mixed with the envelope in first dredge up, enhancing N and depleting C (Iben 1967; Vincenzo et al. 2021; Karakas & Lattanzio 2014). RGB stars thus require model-dependent corrections to recover surface abundances (e.g. Vincenzo et al. 2021). On the other hand, gravitational settling can affect main sequence stellar abundances (e.g. Souto et al. 2019). Subgiants have well-mixed envelopes, so gravitational settling is not as significant, and subgiants have not yet experienced first dredge up. We use a sample of APOGEE DR17 stars (Majewski et al. 2017) as selected in Roberts et al. (2023, in prep.). The selection criteria and differences between the samples are described in more detail in Appendix A.

When plotting the data and models, we bin by groups of 500 (or 150) stars in [Mg/H] ([Mg/Fe]). When plotting [C/Mg]-[Mg/H], we select only the low-α sequence. For [C/Mg]-[Mg/Fe], we instead select stars with $-0.15 \leq$ [Mg/H] ≤ -0.05. To create a sample with similar characteristics of the subgiant observations, we sample 12,000 stars from the simulations such that the cumulative distribution function of stars in R_{gal} is the same for the subgiants and our comparison sample.

5.3 High-Mass Stellar Yields

CCSNe, which we assume make up the majority of C, set the overall C abundance trends. The top of Fig. 8 shows models with varying y_C^{cc} metallicity dependence, ζ^{cc}. As the [C/Mg]-[Mg/H] trend is approximated by equilibrium trends, the models with higher ζ^{cc} also have a steeper slope in [C/Mg]-[Mg/H]. However, [C/Mg]-[Mg/Fe] is minimally affected by changes to ζ^{cc} since CCSNe occurs on much shorter timescales than SNe Ia and AGB enrichment. The only effects on [C/Mg]-[Mg/Fe], when considering the narrow metallicity slice, are because of either the slight change in equilibrium abundances, the imperfect evolution of the galaxy, or that the interstellar medium abundances are set by stars which were born at poorer metallicities. Hence, [C/Mg]-[Mg/H] tells us about the total C yield with metallicity, which [C/Mg]-[Mg/Fe] is independent of. If we know the AGB C yields, then with observed [C/Mg]-[Mg/Fe] abundance trends, we can infer the CCSNe C yields with metallicity.

5.4 Low-Mass Stellar Yields

[C/Mg]-[Mg/Fe] is sensitive to the assumptions about delayed C from AGB stars. If no C comes from low-mass stars, then [C/Mg] would be independent of [Mg/Fe], only [Mg/H]. Instead, C shows strong trends in [C/Mg]-[Mg/Fe] independent of metallicity.

In the middle row of Fig. 8, we first show the four C yield models (K10, K16, C11, V13). For the most part, the AGB yield sets result in qualitatively similar predictions. V13, however, does not reproduce solar trends as the model predicts strong C production at slightly above solar metallicities, resulting in a decreasing [C/Mg] with [Fe/Mg]. As all AGB models predict some low-mass C destruction, each model does predict a downturn in [C/Mg] as [Fe/Mg] increases. A recent burst in star formation may hide this downturn (see section 5.5), but the C destruction is not supported directly by observations.

We also investigate adjustments to the AGB yield fraction f_{agb} The bottom of Fig. 8 shows three models with different AGB fractions while using C11 yields. The [C/Mg]-[Mg/Fe] relationship is set by f_{agb} because a specific amount of C must be released at a delayed time to match the SNe Ia production of Fe and increase [C/Mg] as [Mg/Fe] decreases to reproduce the data. Increased f_{agb} results in a decreased slope in [C/Mg]-[Mg/H], owing to the negative metallicity dependence of y_C^{agb}. So while [C/Mg]-[Mg/H] alone cannot differentiate models which vary f_{agb} and ζ correspondingly, [C/Mg]-[Mg/Fe] provides information on f_{agb}. So, we can use [C/Mg]-[Mg/Fe] to estimate $f_{agb} \approx 0.2$, and then choose ζ to match [C/Mg]-[Mg/H].

Finally, in the top row of Fig. 9, we plot variations of the analytic AGB models (Eqns. 13 and 15) where C production occurs in different mass ranges. If all C comes from stars with masses $> 4 M_\odot$, then [C/Mg] is almost independent of [Fe/Mg]. On the other hand, if all C comes from stars with masses between 1 and 2 M$_\odot$, then [C/Mg] increases across almost the whole range of [Fe/Mg]. As the observed trend in [C/Mg]-[Mg/Fe] is almost linear, then the delay-time-distribution of C is similar to Fe, so C is likely produced in
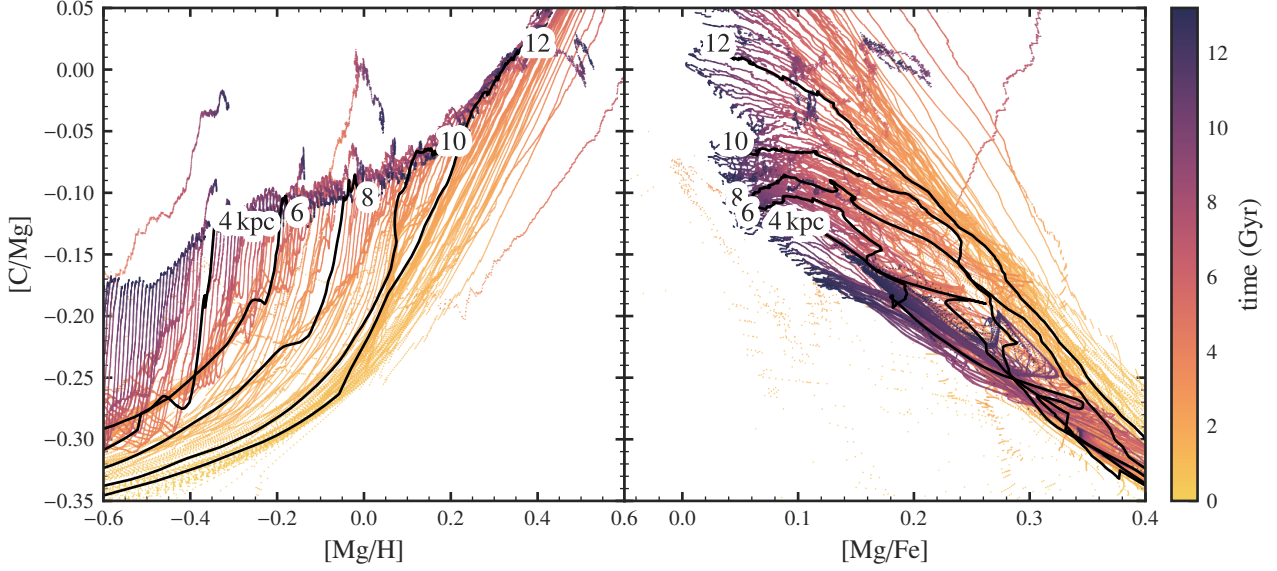
Figure 6. Time evolution of gas-phase C abundances in our fiducial model. Each line represents a zone at a different galactic radii. The lines are coloured-coded by time. The left shows [C/Mg]-[Mg/H] and the right [C/Mg]-[Mg/Fe]. We artificially restrict the axis range in each case to better see solar-annulus and present-day evolution. <UPDATE, CHECK LEFT?RIGHT USAGE>
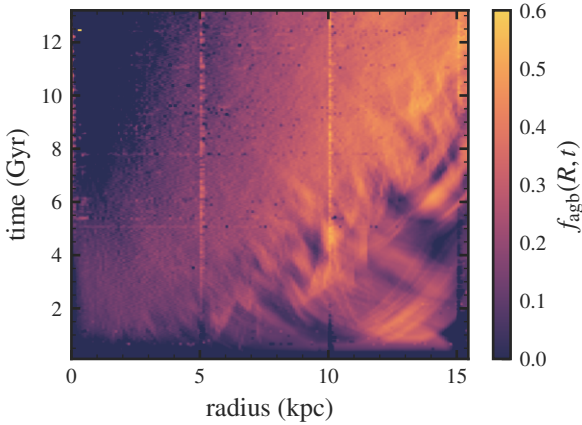

Figure 7. The evolution of f_{agb} across the Galaxy and with time.

a mix of stars between 1 and $4 M_\odot$. We cannot constrain upper-intermediate AGB C production as this behaves similar to CCSNe C.

5.5 Star Formation History and Outflows

In this section, we consider two modifications of our fiducial SFH: *lateburst* and *earlyburst*. Our lateburst model adds a Gaussian factor to the inside-out SFH,

$$\dot{\Sigma}_{\text{lateburst}} \propto \dot{\Sigma}_{\text{inside-out}} \left(1 + A\, e^{-(t-\tau_{\text{burst}})^2/2\sigma_{\text{burst}}^2}\right) \quad (21)$$

where $A = 1.5$ represents the amplitude of the birth, $\tau_{\text{burst}} = 10.8\,\text{Gyr}$ is the time where the burst is strongest, and $\sigma_{\text{burst}} = 1\,\text{Gyr}$ is the width of the burst. Our earlyburst model is instead a double exponential,

with the second exponential begining at $t_1 = 5\,\text{Gyr}$.

$$\dot{\Sigma}_{\text{earlyburst}} \propto A\, e^{-t/\tau_{\text{burst}}} + \begin{cases} e^{-(t-t_1)/\tau_{\text{sfh}}} & t_1 < t \\ 0 & t < t_1 \end{cases} \quad (22)$$

where we take the burst duration, $\tau_{\text{burst}} = 2\,\text{Gyr}$. This approximately corresponds to the Gaia-Encelidus merger, inducing higher star formation in the Milky Way (Spitoni et al. 2021; Bonaca et al. 2020; Helmi et al. 2018).

The middle row of Fig. 9 shows three models with our alternate SFH. Changes to the SFH leave [C/Mg]-[Mg/H] unchanged, but they do introduce slight variation in [C/Mg]-[Mg/Fe]. Models with higher AGB fractions are more sensitive to variations in the SFH. The late burst models result in [C/Mg] continuing to increase at low [Mg/Fe], but also introduce a dip not present in the data. Additionally, the early-burst reproduces the slight break between the low and high α sequences, but overshoots equilibrium more severely than the fiducial model. In general, any of these SFHs are consistent with this model.

The middle row of Fig. 9 also shows a model where η and yields are decreased by a factor 0.3. While changing the value of η affects the metallicity distribution of stars, the model still evolves along the same paths. Our model is unable to differentiate a uniform decrease in both outflows and yields.

5.6 Degeneracies

GCE models of the Milky Way fall into two classes—those which incorporate significant mass-loading (e.g., this work) and those which neglect mass-loading but lower effective yield to match observed abundances (e.g. Minchev et al. 2013, 2014; Spitoni et al. 2019, 2020, 2021). An increase in stellar yields has a nearly identical effect as a decrease in the mass-loading factor η (see Appendix B of Johnson et al. 2022). The equilibrium arguments discussed in Section 3.1 suggest however that abundance ratios are independent of the choice of normalization and the value of η. We, therefore, expect our results regarding the relative yield y_C/y_{Mg} and its metallicity dependence
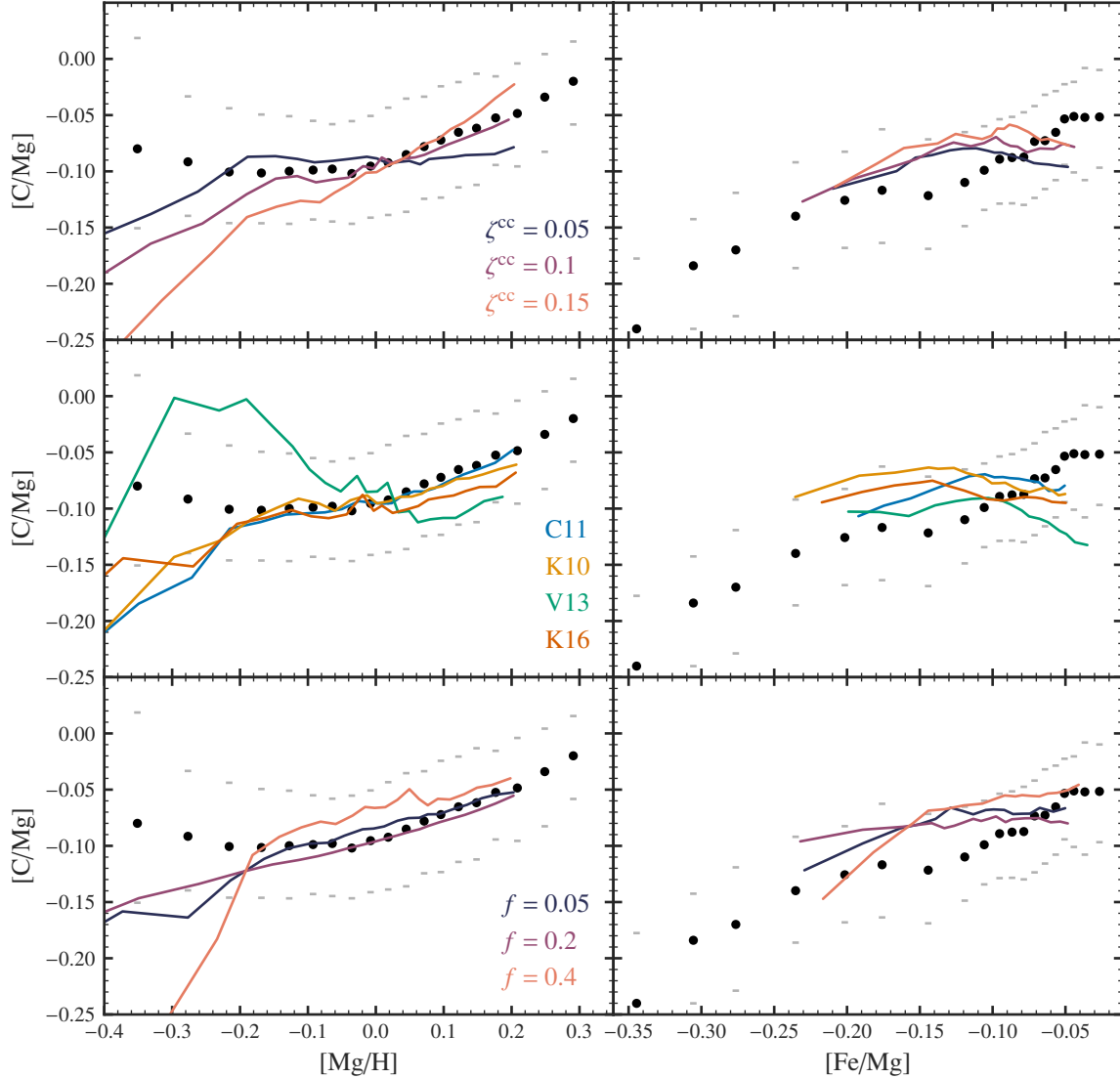
Figure 8. Stellar abundance trends in our model, assuming metallicity independent y_C^{cc}. Colored lines quantify the median [C/Mg] in bins of [Mg/H] for our four AGB yield models from the literature (see Section 2.1). Black points and grey dashes represent the median and standard deviations of [C/Mg] for each [Mg/H] bin in the Roberts et al. (2023, in prep.) sample. In the right panel, we show the trends only for stars where $-0.15 \leq$ [Mg/H] ≤ -0.05.

to extend to the other class of models omitting mass loading. We demonstrate this further here.

The theoretical motivation for decreasing yields is the uncertainty in stellar explodability. If fewer high-mass stars explode, then the yields will be reduced by some factor. Additionally, some fraction of supernovae ejecta may be lost directly to an outflow, lowering effective yields. To explore reduced outflow models, we lower both η and all yields by the same factor to leave the equilibrium abundances unchanged.

An addition source of theoretical uncertainty in this result is that the SNe Ia yield and delay time distributions have their own uncertainties. We do compute models (not shown here) where y_{Fe}^{Ia} is varied. Increasing y_{Fe}^{Ia} has a similar affect as decreasing f^{agb}. Here, we only show models with $y_{Fe}^{Ia} = 0.00214$ and a $t^{-1.1}$ delay-time-distribution choices from the fiducial model here.

5.7 Gas-Phase Abundances

As a final test of the model, we compare the model predictions against gas-phase measurements. Fig. 10 shows the fiducial model's gas-phase predictions compared to observations of the Milky Way and extragalactic HII regions, halo stars, and damped Lyman-alpha systems. While obervations in HII regions and Milky Way stars agree that C/O generally increases at near-solar metallicities, damped Lyman-alpha systems and metal poor stars imply that C/O may also increase again at very low metallicities.

Measurements of C abundances are challenging. In HII regions, C/O abundance ratios are measured with either recombination lines or collisional excitation lines. While broad consistancy of our model with gas-phase measurments is promising, the large measurment errors limit the evaluative power of HII regions. We additionally include Milky Way thick disk (high-α) and halo stars, which span a larger range of metallicities than thin disk stars. However, metal-poor abundance measurements require consideration of 3D-NLTE effects,
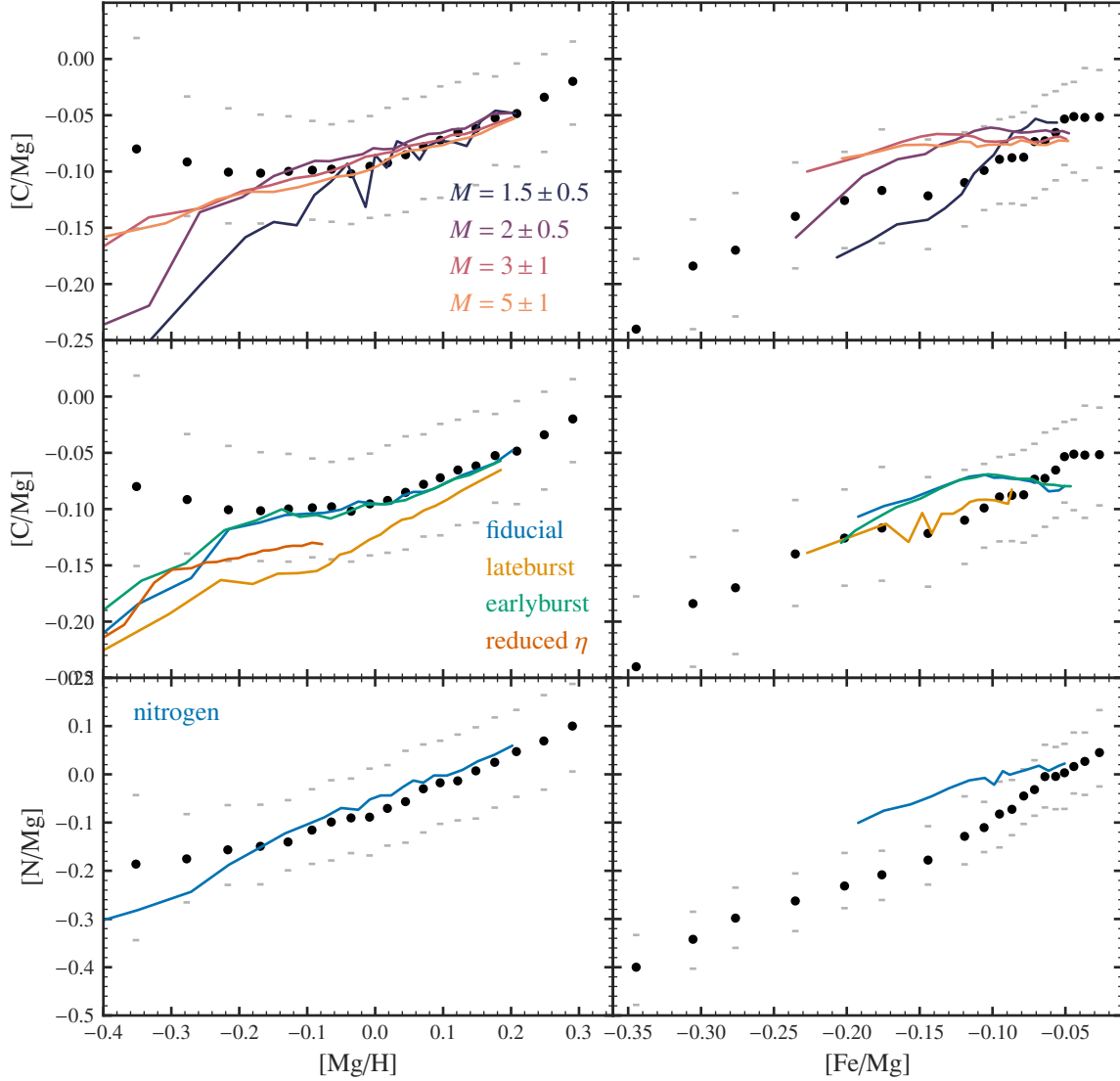
Figure 9. Similar to Fig. 8, except where the AGB C contribution is varied from the fiducial ($f_{\rm agb} = 0.2$) to 0.1 and 0.3 (see Eq. 11 and Section. 5.4).

which can be an ~0.2 dex effect (e.g. CITE). Finally, dwarf galaxies, damped Lyman-alpha systems, and extragalactic regions may represent different SFHs than the Milky Way. As AGB C production is sensitive to variations in the SFH, these environments may not exactly match our subgiant sample, limiting the usefulness of these abundance measurements in evaluating our model.

Fig. 10 shows the single-zone model and time-slices of the fiducial multi-zone model at present day and $t = 2$ Gyr. Here, we consider a single-zone model with parameters consistant with the Gaia-Encelidus sausage[13]. We chose the model to have mass loading $\eta = 6$, star formation efficiency $\tau_\star = 9$ Gyr, and a star formation history $\propto e^{-t/2\,{\rm Gyr}}$, evolved for 6 Gyr. The single-zone model is better able to replicate the slope of the abundances in dwarf galaxies, HII-regions, and halo stars. The single-zone model does not produce an equilibrium track, unlike the multi-zone models. As the single-zone model also evolves slower, the late contribution of AGB stars causes the steeper slope at near-solar metallicities. By including an increase of C yields at low-metallicity, the single-zone model is also able to reproduce the increasing [C/O] abundances with decreasing

metallicity past [O/H] < −1.5. In any case, there is large scatter in the measurments, which both models fall within.

6 CONCLUSIONS

In this work, we investigated the role of C yields on the predictions of multi-zone GCE models. We began by adopting an equilibrium approximation to estimate the total C yields with metallicity from APOGEE subgiant [C/Mg]-[Mg/H] trends. We find that $y_C/y_O = 1/3 + 4(Z - Z_\odot)$ and $y_C/y_{\rm Mg} = 2.7 + 32(Z - Z_\odot)$, where we assume [Mg/O] = 0. We show that [C/Mg]-[Mg/H] is a diagnostic for total C yields with metallicity, but [C/Mg]-[Mg/Fe] provides information about delayed C production. From the [C/Mg]-[Mg/Fe] trends, we estimate that AGB stars with masses between about 1 and 3 M$_\odot$

---

[13] See e.g. CITATION. Th Gaia-Encelidus sausage (GSE) is a kinematically and chemically distinct group of halo stars consistant with the merger of a dwarf galaxy early in the Milky Way's formation.
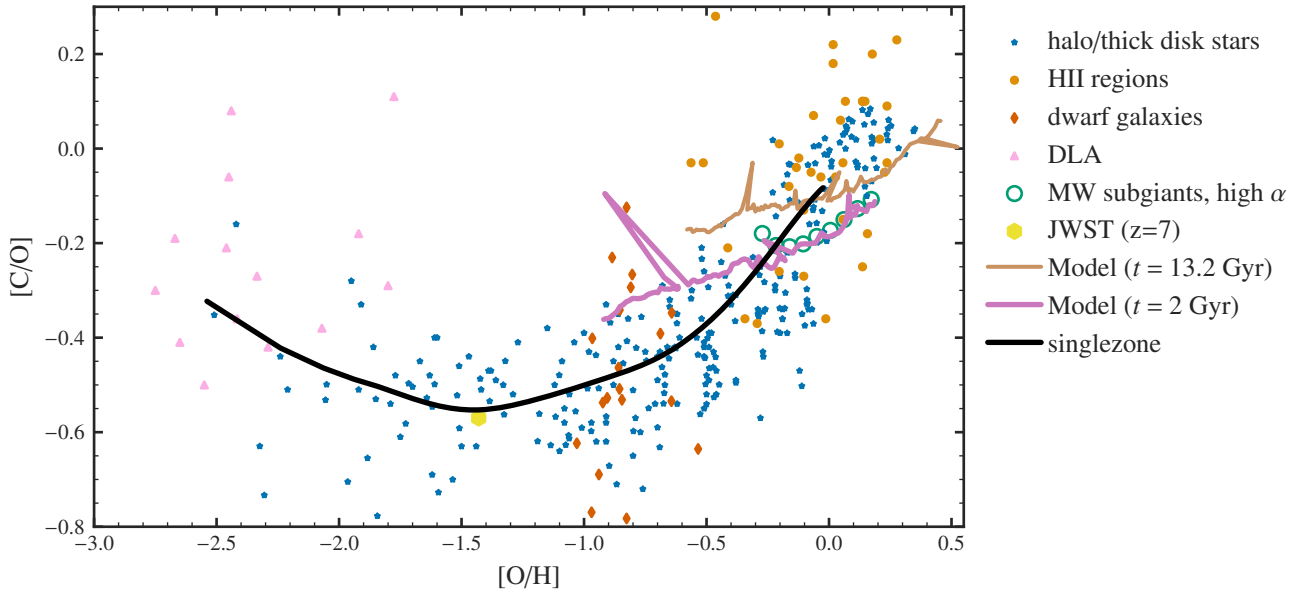
Figure 10. Gas-phase C abundances. We plot our model at $t = 2$ Gyr and present day as thick solid lines. Points represent measurements in HII regions (pink circles; Skillman et al. 2020; Esteban et al. 2002, 2009, 2014, 2019) damped Lyman-alpha (DLA) systems (blue triangles; Ellison et al. 2010; Srianand et al. 2010; Dutta et al. 2014; Dessauges-Zavadsky et al. 2003; Pettini et al. 2008; Morrison et al. 2016; Cooke et al. 2017), dwarf galaxies (red diamonds; Berg et al. 2019), Milky Way halo and thick disk stars (green stars; Nissen et al. 2014; Fabbian et al. 2009), and Milky Way high-α stars (yellow points; Robert et al. 2023, in prep.). (OUT OF DATE)

contribute ~20% of total C abundances. In this model, the remaining ~80% of C comes from high-mass stars with a metallicity dependent yield of $y_C^{cc}/y_{Mg} = 2.2 + 55(Z/Z_\odot)$, broadly consistant with rotating CCSNe models.

We additionally explore variations of the assumed SFH and outflow mass-loading factor η. We find that alternate SFHs can perturb [C/Mg]-[Mg/Fe]and [C/Mg]-[Mg/H] abundances slightly. Decreasing both outflows and yields by the same factor leaves the [C/Mg]-[Mg/H] and [C/Mg]-[Mg/Fe] trends unaffected, ingoring effect to the metalliticy distribution of starrs. These constraints on the relative yields of C, O, and Mg are robust against variations in η.

Finally, we compare our model against gas-phase measurements and Milky Way halo stars. By including yields which are enhanced at low metallicities, CCSNe and AGB stars together are able to explain the general trends of C from metallicities of [O/H] = −3 to 0.5.

Our C yield constraints provide a useful benchmark for stellar evolution models. C yields are sensitive to poorly understood processes, including mass-loss prescriptions, explodability, nuclear cross sections, convection, and stellar structure. Future spectroscopic surveys combined with Gaia kinematics (Gaia Collaboration et al. 2016) will continue to enhance our understanding of chemical evolution. Both the Sloan Digital Sky Survey V's Milky Way Mapper program (SDSS-V/MWM) (Kollmeier et al. 2017) and the Dark Energy Spectroscopic Instrument (DESI) Milky Way survey (DESI Collaboration et al. 2016; Cooper et al. 2022) will each measure spectra of upwards 6,000,000 Milky Way stars. These larger samples will enable similar work to tighten constraints on stellar models and our understanding of galaxy structure and evolution.

DATA AVAILABILITY

The inclusion of a Data Availability Statement is a requirement for articles published in MNRAS. Data Availability Statements provide a standardised format for readers to understand the availability of data underlying the research results described in the article. The statement may refer to original data generated in the course of the study or to third-party data analysed in the article. The statement should describe and provide means of access, where possible, by linking to the data or providing the required accession numbers for the relevant databases or DOIs.

REFERENCES

Abdurro'uf et al., 2022, ApJS, 259, 35
Adelberger E. G., et al., 2011, Reviews of Modern Physics, 83, 195
Asplund M., Grevesse N., Sauval A. J., Scott P., 2009, ARA&A, 47, 481
Astropy Collaboration et al., 2013, A&A, 558, A33
Astropy Collaboration et al., 2018, AJ, 156, 123
Astropy Collaboration et al., 2022, ApJ, 935, 167
Bensby T., Feltzing S., 2006, MNRAS, 367, 1181
Berg D. A., Erb D. K., Henry R. B. C., Skillman E. D., McQuinn K. B. W., 2019, ApJ, 874, 93
Bird J. C., Kazantzidis S., Weinberg D. H., 2012, MNRAS, 420, 913

Bird J. C., Kazantzidis S., Weinberg D. H., Guedes J., Callegari S., Mayer L., Madau P., 2013, ApJ, 773, 43

Bird J. C., Loebman S. R., Weinberg D. H., Brooks A. M., Quinn T. R., Christensen C. R., 2021, MNRAS, 503, 1815

Bland-Hawthorn J., Gerhard O., 2016, ARA&A, 54, 529

Bonaca A., et al., 2020, ApJ, 897, L18

Brooks A. M., Zolotov A., 2014, ApJ, 786, 87

Chiappini C., Romano D., Matteucci F., 2003, MNRAS, 339, 63

Christensen C., Quinn T., Governato F., Stilp A., Shen S., Wadsley J., 2012, MNRAS, 425, 3058

Cooke R. J., Pettini M., Steidel C. C., 2017, MNRAS, 467, 802

Cooper A. P., et al., 2022, arXiv e-prints, p. arXiv:2208.08514

Cristallo S., et al., 2011, ApJS, 197, 17

Cristallo S., Straniero O., Piersanti L., Gobrecht D., 2015, ApJS, 219, 40

DESI Collaboration et al., 2016, arXiv e-prints, p. arXiv:1611.00036

Dalcanton J. J., 2007, ApJ, 658, 941

Dearborn D. S. P., Tinsley B. M., Schramm D. N., 1978, ApJ, 223, 557

Dessauges-Zavadsky M., Péroux C., Kim T. S., D'Odorico S., McMahon R. G., 2003, MNRAS, 345, 447

Dutta R., Srianand R., Rahmani H., Petitjean P., Noterdaeme P., Ledoux C., 2014, MNRAS, 440, 307

Ellison S. L., Prochaska J. X., Hennawi J., Lopez S., Usher C., Wolfe A. M., Russell D. M., Benn C. R., 2010, MNRAS, 406, 1435

Esteban C., Peimbert M., Torres-Peimbert S., Rodríguez M., 2002, ApJ, 581, 241

Esteban C., Bresolin F., Peimbert M., García-Rojas J., Peimbert A., Mesa-Delgado A., 2009, ApJ, 700, 654

Esteban C., García-Rojas J., Carigi L., Peimbert M., Bresolin F., López-Sánchez A. R., Mesa-Delgado A., 2014, MNRAS, 443, 624

Esteban C., García-Rojas J., Arellano-Córdova K. Z., Méndez-Delgado J. E., 2019, arXiv e-prints, p. arXiv:1905.10129

Fabbian D., Nissen P. E., Asplund M., Pettini M., Akerman C., 2009, A&A, 500, 1143

Finlator K., Davé R., 2008, MNRAS, 385, 2181

Franchini M., et al., 2020, ApJ, 888, 55

Frankel N., Rix H.-W., Ting Y.-S., Ness M., Hogg D. W., 2018, ApJ, 865, 96

Frankel N., Sanders J., Ting Y.-S., Rix H.-W., 2020, ApJ, 896, 15

Frinchaboy P. M., et al., 2013, ApJ, 777, L1

Gaia Collaboration et al., 2016, A&A, 595, A1

García Pérez A. E., et al., 2016, AJ, 151, 144

García-Rojas J., Esteban C., 2007, ApJ, 670, 457

Gilroy K. K., 1989, ApJ, 347, 835

Griffith E. J., Sukhbold T., Weinberg D. H., Johnson J. A., Johnson J. W., Vincenzo F., 2021, ApJ, 921, 73

Harris C. R., et al., 2020, Nature, 585, 357

Hasselquist S., et al., 2019, ApJ, 871, 181

Hayden M. R., et al., 2014, AJ, 147, 116

Helmi A., Babusiaux C., Koppelman H. H., Massari D., Veljanoski J., Brown A. G. A., 2018, Nature, 563, 85

Henry R. B. C., Edmunds M. G., Köppen J., 2000, ApJ, 541, 660

Hunter J. D., 2007, Computing in Science & Engineering, 9, 90

Iben Icko J., 1967, ARA&A, 5, 571

Isern J., 2019, ApJ, 878, L11

Johnson J. A., 2019, Science, 363, 474

Johnson J. W., Weinberg D. H., 2020, MNRAS, 498, 1364

Johnson J. W., et al., 2021, MNRAS, 508, 4484

Johnson J. W., et al., 2022, arXiv e-prints, p. arXiv:2210.01816

Johnson J. W., Weinberg D. H., Vincenzo F., Bird J. C., Griffith E. J., 2023, MNRAS, 520, 782

Karakas A. I., 2010, MNRAS, 403, 1413

Karakas A. I., Lattanzio J. C., 2014, Publ. Astron. Soc. Australia, 31, e030

Karakas A. I., Lugaro M., 2016, ApJ, 825, 26

Karakas A. I., Lugaro M., Carlos M., Cseh B., Kamath D., García-Hernández D. A., 2018, MNRAS, 477, 421

Kennicutt Robert C. J., 1998, ARA&A, 36, 189

Kobayashi C., Karakas A. I., Lugaro M., 2020, ApJ, 900, 179

Kollmeier J. A., et al., 2017, arXiv e-prints, p. arXiv:1711.03234

Korn A. J., Grundahl F., Richard O., Mashonkina L., Barklem P. S., Collet R., Gustafsson B., Piskunov N., 2007, ApJ, 671, 402

Kroupa P., 2001, MNRAS, 322, 231

Laird J. B., 1985, ApJ, 289, 556

Lambert D. L., Ries L. M., 1981, ApJ, 248, 228

Lambert D. L., Gustafsson B., Eriksson K., Hinkle K. H., 1986, ApJS, 62, 373

Larson R. B., 1972, Nature Physical Science, 236, 7

Larson R. B., 1974, MNRAS, 166, 585

Licquia T. C., Newman J. A., 2015, ApJ, 806, 96

Lilly S. J., Carollo C. M., Pipino A., Renzini A., Peng Y., 2013, ApJ, 772, 119

Limongi M., Chieffi A., 2018, ApJS, 237, 13

Lind K., Korn A. J., Barklem P. S., Grundahl F., 2008, A&A, 490, 777

Loebman S. R., Ivezić Ž., Quinn T. R., Governato F., Brooks A. M., Christensen C. R., Jurić M., 2012, ApJ, 758, L23

Majewski S. R., et al., 2017, AJ, 154, 94

Maoz D., Mannucci F., Brandt T. D., 2012, MNRAS, 426, 3282

Martig M., et al., 2016, MNRAS, 456, 3655

Masseron T., Gilmore G., 2015, MNRAS, 453, 1855

Matteucci F., 2021, A&ARv, 29, 5

Minchev I., Chiappini C., Martig M., 2013, A&A, 558, A9

Minchev I., Chiappini C., Martig M., 2014, A&A, 572, A92

Mor R., Robin A. C., Figueras F., Roca-Fàbrega S., Luri X., 2019, A&A, 624, L1

Morrison S., Kulkarni V. P., Som D., DeMarcy B., Quiret S., Péroux C., 2016, ApJ, 830, 158

Nissen P. E., Chen Y. Q., Carigi L., Schuster W. J., Zhao G., 2014, A&A, 568, A25

Nomoto K., Kobayashi C., Tominaga N., 2013, ARA&A, 51, 457

Ohio Supercomputer Center 1987, Ohio Supercomputer Center, http://osc.edu/ark:/19495/f5s1ph73

Pagel B. E. J., 2009, Nucleosynthesis and Chemical Evolution of Galaxies, 2 edn. Cambridge University Press, doi:10.1017/CBO9780511812170

Peeples M. S., Shankar F., 2011, MNRAS, 417, 2962

Pérez F., Granger B. E., 2007, Computing in Science and Engineering, 9, 21

Pettini M., Zych B. J., Steidel C. C., Chaffee F. H., 2008, MNRAS, 385, 2011

Prantzos N., Abia C., Limongi M., Chieffi A., Cristallo S., 2018, MNRAS, 476, 3432

Romano D., 2022, A&ARv, 30, 7

Romano D., Karakas A. I., Tosi M., Matteucci F., 2010, A&A, 522, A32

Rybizki J., Just A., Rix H.-W., 2017, A&A, 605, A59

Sánchez S. F., 2020, ARA&A, 58, 99

Sellwood J. A., Binney J. J., 2002, MNRAS, 336, 785

Skillman E. D., Berg D. A., Pogge R. W., Moustakas J., Rogers N. S. J., Croxall K. V., 2020, ApJ, 894, 138

Souto D., et al., 2018, ApJ, 857, 14

Souto D., et al., 2019, ApJ, 874, 97

Spitoni E., Silva Aguirre V., Matteucci F., Calura F., Grisoni V., 2019, A&A, 623, A60

Spitoni E., Verma K., Silva Aguirre V., Calura F., 2020, A&A, 635, A58

Spitoni E., et al., 2021, A&A, 647, A73

Srianand R., Gupta N., Petitjean P., Noterdaeme P., Ledoux C., 2010, MNRAS, 405, 1888

Sukhbold T., Ertl T., Woosley S. E., Brown J. M., Janka H. T., 2016, ApJ, 821, 38

Tacconi L. J., et al., 2018, ApJ, 853, 179

Tinsley B. M., 1979, ApJ, 229, 1046

Tinsley B. M., 1980, Fundamentals Cosmic Phys., 5, 287

Ventura P., Di Criscienzo M., Carini R., D'Antona F., 2013, MNRAS, 431, 3642

Ventura P., Dell'Agli F., Schneider R., Di Criscienzo M., Rossi C., La Franca F., Gallerani S., Valiante R., 2014, MNRAS, 439, 977

Ventura P., Karakas A., Dell'Agli F., García-Hernández D. A., Guzman-Ramirez L., 2018, MNRAS, 475, 2282

Ventura P., Dell'Agli F., Lugaro M., Romano D., Tailo M., Yagüe A., 2020, A&A, 641, A103

Vincenzo F., et al., 2021, arXiv e-prints, p. arXiv:2106.03912

Virtanen P., et al., 2020, Nature Methods, 17, 261
Waskom M. L., 2021, Journal of Open Source Software, 6, 3021
Weinberg D. H., Andrews B. H., Freudenburg J., 2017, ApJ, 837, 183
Weinberg D. H., et al., 2019, ApJ, 874, 102
Weinberg D. H., et al., 2022, ApJS, 260, 32
Woosley S. E., Weaver T. A., 1995, ApJS, 101, 181
Zolotov A., et al., 2012, ApJ, 761, 71
pandas development team T., 2020, pandas-dev/pandas: Pandas, doi:10.5281/zenodo.3509134, https://doi.org/10.5281/zenodo.3509134

APPENDIX A: THE SUBGIANT SAMPLE

As the primary observational constraint, we use the criteria outlined in Roberts et al. (2023, in prep.) to create a sample of subgiant from APOGEE DR17 (Majewski et al. 2017). apogee is part of the Sloan Digital Sky Survey and measures high-resolution spectra of thousands of stars Abdurro'uf et al. (2022). Chemical abundances are determined from the APOGEE Stellar Parameter and Chemical Abundance Pipeline (ASPCAP) (García Pérez et al. 2016).

Photospheric C and N abundances in subgiant are reflective of their birth abundances (Gilroy 1989; Korn et al. 2007; Lind et al. 2008; Souto et al. 2018, 2019) As first dredge up, which affects C and N abundances, only occurs during the ascent onto the RGB, subgiant stars are unaffected by this enrichment.

An alternate approach for this analysis would be to estimate the birth abundances of RGB stars by correcting surface abundance effects from first dredge up as in Vincenzo et al. (2021). Subgiants are the more attractive option since these observations do not rely on model-dependent corrections. However, RGB stars are more luminous, potentially allowing better coverage of the Galactic disk.

We choose to use Roberts et al. (2023, in prep.) sample as this does not rely on additional layers of modeling, providing a more direct constraint to our model and limiting our systematic uncertainties.

Fig. A1 shows a plot of all APOGEE stars and the Roberts et al. (2023, in prep.)polygon selection criteria. Roberts et al. (2023, in prep.) select a region of stars based on surface gravity $\log g$, and effective surface temperature, $T_{\rm eff}$.

$$
\begin{cases}
\log g \geq 3.5 \\
\log g \leq 0.004\, T_{\rm eff} - 15.7 \\
\log g \leq 0.000706\, T_{\rm eff} + 0.36 \\
\log g \leq -0.0015\, T_{\rm eff} + 12.05 \\
\log g \geq 0.0012\, T_{\rm eff} - 2.8.
\end{cases}
\tag{A1}
$$

Additionally, we included stars in APOGEE marked by the following flags.

- APOGEE_MIRCLUSTER_STAR
- APOGEE_EMISSION_STAR
- APOGEE_EMBEDDEDCLUSTER_STAR
- young cluster (IN-SYNC)
- APOGEE2_W345
- EB planet

This cut isolates a clean sample of ~12,000 subgiants. We furthermore isolate the low- and high-α sequences with the cut

$$
\begin{cases}
[{\rm Mg/Fe}] > 0.12 - 0.13\,[{\rm Fe/H}], & [{\rm Fe/H}] < 0 \\
[{\rm Mg/Fe}] > 0.12, & [{\rm Fe/H}] > 0.
\end{cases}
\tag{A2}
$$

The low-α sequence is better reproduced by this model, so we use this cut of the subgiants to compare the models against except for comparing [C/Mg]-[Mg/Fe].
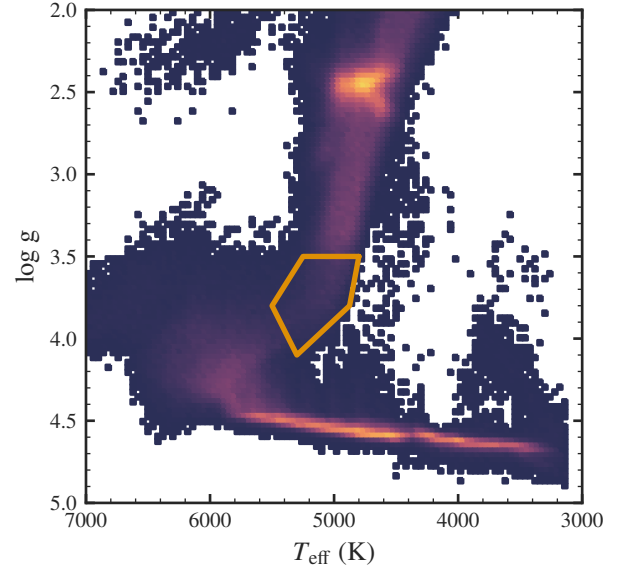
Figure A1. A Kiel diagram of APOGEE stars. Following Roberts et al. (2023, in prep.), we select subgiants in the orange polygon (see Equation A1). These stars have not yet experienced first dredge-up, so their photospheric C and N abundances should reflect their birth mixture.

APPENDIX B: AGB YIELD MODELS

A brief summary of the four AGB models we consider, the masses and metallicites of each yield set, and differences between the models.

C11. Yields from Cristallo et al. (2011, 2015). Models include masses 1.3, 1.5, 2.0, 2.5, 3.0, 4.0, 5.0, and 6.0 $M_\odot$; and metallicities $Z = 0.0001, 0.0003, 0.001, 0.002, 0.003, 0.006, 0.008, 0.01, 0.014, 0.02$. C11 uses a higher triple-α reaction rate than others and has weaker hot bottom burning, so

K10. Yields are published in Karakas (2010). Models include masses 1.0, 1.25, 1.5, 1.75, 1.9, 2.25, 2.5, 3.0, 3.5, 4.0, 4.5, 5.0, 5.5, 6.0 $M_\odot$; and metallicities $Z = 0.0001, 0.004, 0.008, 0.02$. K10 use an ad-hoc mass-loss prescription which likely is not physical as opacities are poorly understood. K10 also has a lower temperature at the base of the convective envelope so hot bottom burning is not as strong as other models, likely explaining why low-metallicity C yields are higher.

V13 Yields are published in Ventura et al. (2013, 2014, 2018); Vincenzo et al. (2021), Models include masses 1.5, 2.0, 2.5, 3.0, 3.5, 4.0, 4.5, 5.0, 6.0, 6.5, 7.0 $M_\odot$; and metallicities $Z = 0.0003, 0.001, 0.002, 0.004, 0.008, 0.014, 0.04$. V13is evololved with DHFJKSLDF, V13is unusual in that hot bottom burning is much stronger than other models due to more efficient convection and higher temperatures at the base of the convective envelope, resulting in much lower stellar yields and negative yields above solar metallicities.

K16 Yields are published in Karakas & Lugaro (2016); Karakas et al. (2018) Models include masses 1.0, 1.25, 1.5, 1.75, 2.25, 2.5, 2.75, 3.0, 3.25, 3.5, 3.75, 4.0, 4.5, 5.0, 5.5, 6.0, 7.0 $M_\odot$; and metallicities $Z = 0.0003, 0.001, 0.002, 0.004, 0.008, 0.014, 0.04$. This yield set was extended up to metallicities of 0.1 in DFJSD; however, we do not consider this range here. K16 has stronger dredge up than C11, but lower 3-alpha reaction rates. However, K16 has more rapid puses and stays higher mass for longer. HBB is stronger at high mass than C11.

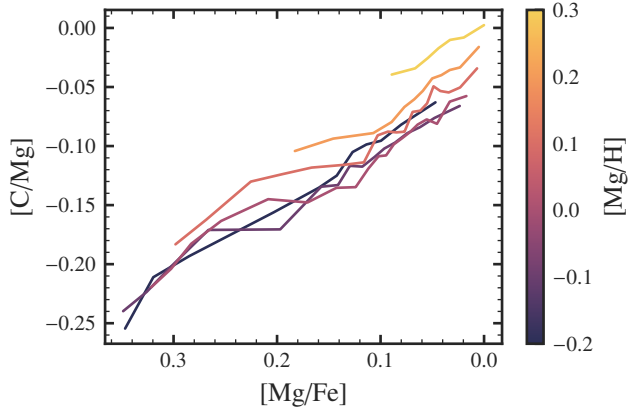This paper has been typeset from a TEX/LATEX file prepared by the author.

Figure B1. hello